applied sciences

MDPI

Article

Mid-Infrared Grayscale Metasurface Holograms

Kedi Wu [1], Nicolas Kossowski [2], Haodong Qiu [2], Hong Wang [2], Qijie Wang [2,*] and Patrice Genevet [3,*]

1 School of Science, Nanjing University of Science and Technology, Nanjing 210094, China; wukedi0410@gmail.com

2 CINTRA, Nanyang Technological University, Singapore 637553, Singapore; nico.kossowski@gmail.com (N.K.); dreambluestee@gmail.com (H.Q.); ewanghong@ntu.edu.sg (H.W.)

3 Université Côte d'Azur, CNRS, CRHEA, rue Bernard Gregory, Sophia Antipolis, 06560 Valbonne, France

* Correspondence: qjwang@ntu.edu.sg (Q.W.); patrice.genevet@crhea.cnrs.fr (P.G.)

Received: 19 December 2019; Accepted: 9 January 2020; Published: 11 January 2020

check for updates

Abstract: Optical metasurfaces composed of two-dimensional arrays of densely packed nanostructures can project arbitrary holographic images at mid-infrared frequency. Our approach employs silicon nanopillars to control light properties, including polarization-independent phase response working with high-transmission efficiency over the 2π-phase modulation range at wavelength 4.7 μm. We experimentally dispose nanopillars accordingly to phase-only profiles calculated using the conventional Gerchberg–Saxton algorithm and revealed the optical performances of our devices using a mid-infrared on-axis optical setup. The total efficiency of our reflection hologram reaches 81%. Our experimental results agree well with the image of the desired object, opening up new perspectives for mid-infrared imaging and displaying for military, life science and sensing application.

Keywords: metasurfaces; hologram; mid-infrared optics

1. Introduction

Recently, ultrathin optical metasurfaces have attracted great interest in optics, offering a new avenue to arbitrarily control electromagnetic waves at mid-IR and optical wavelengths [1,2]. By using subwavelength two-dimensional resonators [3–12], the phase, amplitude, polarization and dispersion of light can be controlled locally [3]. Although earlier works and many functional metasurfaces are based on plasmonic nanostructures, they usually suffer from low efficiency due to intrinsic loss and limited control on the type of resonances involved in the scattering of light [9]. In contrast, dielectric nanostructures based on Mie resonances possess richer modal response to not only locally controlling the light field but also avoiding absorption loss [10–16]. Leveraging on low-loss dielectric units and arranging the abrupt phase and amplitude profiles in various patterns, functional optical devices such as flat lenses [17,18], wave plates [19,20] and holograms [21–24] have been demonstrated. The former devices, inspired by the pioneering works in diffraction optics, for example, Fresnel lenses, require relatively simple distribution of elements to impart hyperbolic phase delays. The latter components, however, rely on complex phase distribution, generally obtained from the principle of holography. Holographic methods have generally been developed and used for applications such as virtual imaging, making use of interference and diffraction to record phase information of objects directly onto photographic plates. Three-dimensional images of the recorded object can later be projected in free space by diffracting a reading-coherent beam from the holographic plate. This traditional holographic method requires highly spatially coherent light sources and intensity-sensitive recording media to store the above-mentioned interference pattern with sufficient accuracy. Later, computer-generated holograms have been proposed by coding the information of the object into phase distribution at a specific plane [25]. By storing wavelength-scale phase information onto the photographic plate, the hologram efficiency is limited by diffraction effect. Dielectric metasurfaces can instead attain deep subwavelength-phase discretization, providing new opportunities in terms of spatial phase resolution, high efficiency and multifunctionalities [24]. In this paper, we demonstrate a dielectric polarization-independent metasurface hologram working in reflection mode at mid-infrared wavelengths. Relying on the previous work on dielectric metasurfaces utilizing simultaneous excitation of both electric and magnetic dipole resonances [9], we designed silicon (Si) nanopillars on a gold substrate, varying radii to realize 0–2π-phase modulation. The Gerchberg–Saxton (GS) Fourier transform hologram approach was employed as the algorithm to decide the position of our phase elements. The eight-level discretized phase hologram, which allows us to bypass some nanofabrication difficulties, has been realized and experimentally demonstrated using the mid-infrared optical setup.

2. Materials and Methods

The configuration schematic of the hologram unit is illustrated in Figure 1a. The Si pillar with radius R and height H was placed on an optically thick, reflecting gold substrate with period P. In our demonstration, the wavelength of incident light emitted from a quantum cascade laser (Daylight Solutions, MIRcat-QT™) was 4.7 μm. Rough estimation of the position of the first order of Mie resonance gave a resonant wavelength of $\lambda = 2$ nH, where $n = 3.43$ is the refractive index of Si [9,26]. To be in the parameter range to observe and rely on scattering from the first few resonant modes of the dielectric particles, the height of the nanopillar was chosen as 650 nm. The period of the pillars with square lattice was chosen to be subwavelength in free space but not necessarily subwavelength in the substrate with P $=$ 2 μm. Designing properly the resonant response of our scattering elements, the diffracted modes inside the dielectric can be suppressed. To achieve a good phase sampling of our hologram, a 2π variation at the operation wavelength was needed, which was achieved by considering the scattering of light with nanopillars of different radii. Phase and amplitude characterization of the building blocks was performed using the finite-difference time-domain method, considering a normal incident plane wave and characterizing the transmitted fields after reflecting from the interface [27]. Figure 1b shows the simulation results of the reflection phase delay. From this figure, we see that radii ranging from 320 to 920 nm can achieve the 2π variation. The amplitude of the reflection light was nearly 1 of all types of nanopillars due to low loss in Si and almost perfect mirror reflectivity of Au at mid-IR frequency (blue line shown in Figure 1b).

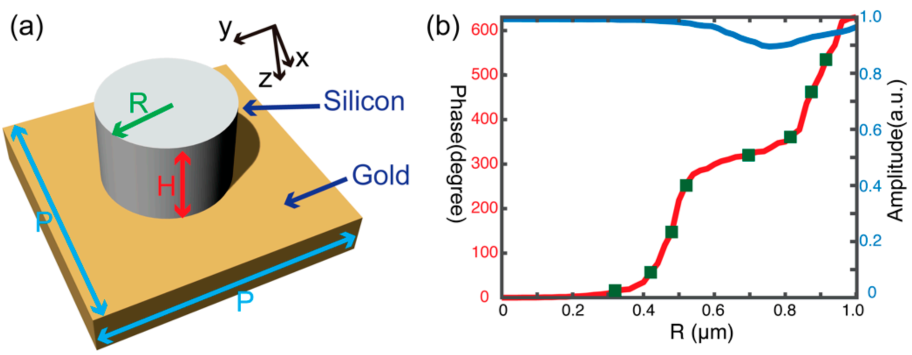

Figure 1. Schematic of the design of the hologram unit. (**a**) Silicon nanopillar with variable radius R and constant period P = 2 μm and height H = 650 nm is placed on the gold substrate. (**b**) Phase shift (red line) and amplitude (blue line) of the reflection light versus the radii of pillar at wavelength 4.7 μm.

Phase-only holograms, for example, an object $I(x, y)$ producing a smile logo, were designed using the iterative Fourier transform algorithm, see Figure 2a. The numerical process used to define the phase distribution works as follows. First, it calculates the Fourier transform (FT) of the object to obtain its angular spectrum, which could be read as $A_0(f_x, f_y)$. The phase profile of $A_0(f_x, f_y)$ is obtained as $A_0\prime(f_x, f_y)$. Second, taking the inverse Fourier transform (iFT) of $A_0\prime(f_x, f_y)$ results in $I_0(x, y)$ with the phase profile $I_0\prime(x,y)$. Taking $I_0\prime(x,y)$ as a new object and repeating the above iteration process several times until $A'_n(f_x,f_y) = A_{n-1}\prime(f_x,f_y)$, where the subscript denotes the iteration time, we obtain the final hologram $B(u,v) = A'_n(f_x,f_y)$, where (u,v) denotes the hologram placed at a different object plane (x,y). Figure 2b shows the phase-only hologram calculated by the above algorithm composed of 2000 iterations. The iterative Fourier transform algorithm implemented in our manuscript follows the flow chart, see Figure 2c.

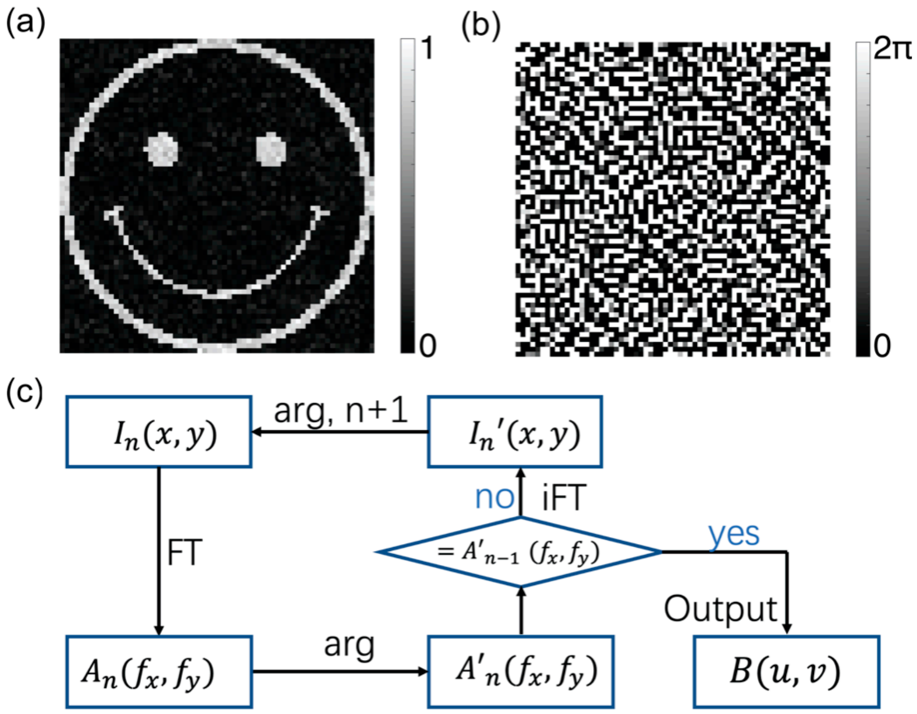

Figure 2. (**a**) Gray intensity distributions of an object $I(x,y)$ to be displayed. (**b**) Calculated phase profile $B(u,v)$ of the phase-only hologram of the object in (a). (**c**) Block diagram of the iterative Fourier transform algorithm used for calculating (b) from (a).

The optical setup built to characterize our devices is shown in Figure 3a. A laser beam from a mid-infrared quantum-cascade laser (4.7 µm, 100 mW) was reflected from the beam splitter and directed to the sample at normal incidence. A CaF_2 lens with a focal length of 5 cm was used to FT the reflected light field. The metasurface hologram was placed in the front foci plane of the lens and a mercury cadmium telluride (MCT) detector utilized in two dimensions to scan the back foci plane and collect the spatial field distribution. The size of the MCT detector was 25 µm, indicating that the minimal spatial resolution of the image was 25 µm. The phase-only hologram shown in Figure 2b was discretized to an eight-level hologram, meaning that 2π-phase variation was divided into 0, $\pi/4$, $\pi/2$, $3\pi/4$, π, $5\pi/4$, $3\pi/2$ and $7\pi/4$ modulation with pillar radii of 320, 420, 480, 560, 720, 820, 880 and 920 nm, respectively.

To fabricate our structure, we started from 180-nm-thick gold film evaporated on a Si wafer using electron-beam (E-beam) evaporation. To increase adhesion of Si on both sides of the gold film, a 10 nm titanium film was evaporated. We then grew a 650-nm-thick amorphous silicon (α-Si) layer using plasma-enhanced chemical-vapor deposition. The holographic pattern was transferred to the Si using E-beam lithography with ZEP520A electron beam resist, spin-coated onto the α-Si layer at 6000 rpm for 90 s. After baking the coated multilayered substrate at 180 °C for 3 min to evaporate the solvent, we obtained 300-nm-thick resist film for electron beam lithography. For patterning the resist, we adjusted the electron beam to an electron dose of 210 µC/cm^2. The exposed resist films were developed in ZED-N50 developer for 60 s at 20 °C. After rinsing in isopropyl alcohol for 30 s and drying by nitrogen flow, the developed resist film with the desired pattern was transferred onto the α-Si using deep reactive-ion etching (RIE) Bosch process in an Oxford Estrelas system. Each cycle of the Bosch process comprised repetition of an etching (SF_6) step of 2 s duration and a sidewall-passivation (C_4F_8) step of 1 s duration. In the etching step, SF_6 gas with the flow of 300 sccm was applied with an inductively coupled plasma (ICP) power of 3000 W in the applied pressure of 120 mTorr. For the passivation step, C_4F_8 gas with the flow of 160 sccm was utilized with an ICP power of 1500 W in the same applied pressure of the etching step. This process cycle was then repeated 22 times until the α-Si was fully etched. The excess of resist was removed by flashing the device into a plasma etcher. The scanning electron microscope (SEM) (LEO 1550 Gemini FESEM) image shown in Figure 3b gives an oblique view of the fabricated hologram. Each pixel of hologram is 10 × 10 μm in size, containing 5 × 5 Si nanopillars. The total hologram contains 64 × 64 pixels. Figure 3c shows a top view of an enlarged area on the hologram. The unit of each scatter is isotropic, thus our present metasurface-based hologram is polarization-independent [28,29].

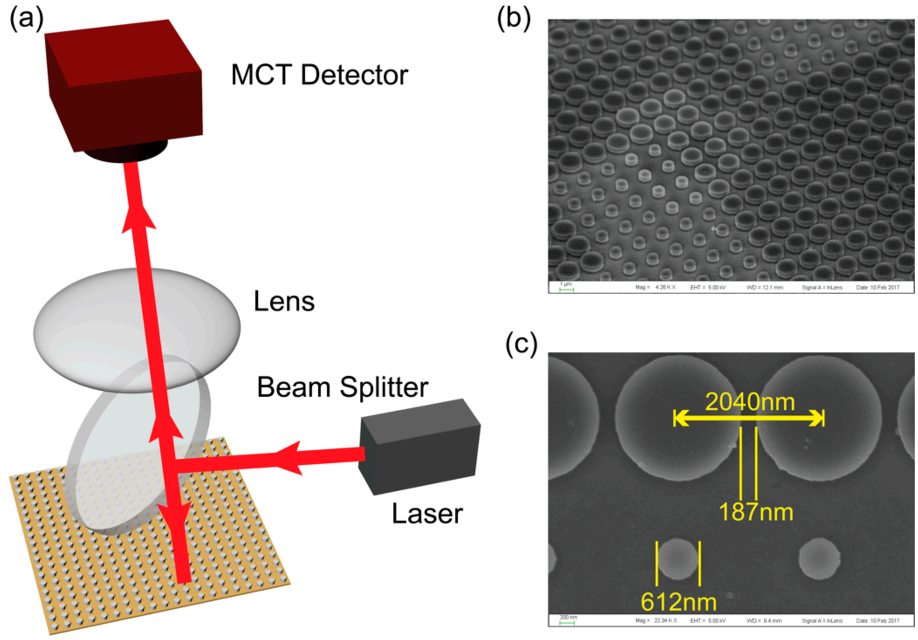

Figure 3. (**a**) Sketch of the on-axis optical scanning experiment setup for demonstration of the hologram. (**b**,**c**) The SEM images of the fabricated hologram in oblique view and top view.

3. Results

The completed hologram in Figure 3a is illuminated by the laser beam impinging on the interface at normal incidence. The far-field calculated image in Figure 4a shows that some information is lost during the far-field projection, as observed after comparing the image quality obtained numerically and the input object in Figure 2a. This is due to the phase discretization. The ideal resolution of the simulated image is 32.5 μm, which is determined by the total size of the hologram, the pixel size of the hologram and the optical resolution of the lens. At the back foci plane of our imaging setup, an MCT detector is attached on a microdisplacement platform with a scanning step of 25 μm for scanning the far-field image of the hologram. The detected image with size 2 × 2 mm is shown in Figure 4b. The image has been experimentally reconstructed by considering point-by-point intensity distribution, and assembling the spatial-intensity distribution to recover our expected smiling logo. Note that the bright nose spot in the center of the image is caused by the zeroth-order diffraction of the hologram sample. From the raw data of the measured image, we estimate that the unwanted zeroth-order perturbation is ~19%, indicating that the total efficiency of our metasurface-based hologram is considerably high, up to 81%. We would like to underline the fact that the reported performance could be further increased, notably by properly considering near-field coupling of metasurface building blocks using optimization design methods [30–35].

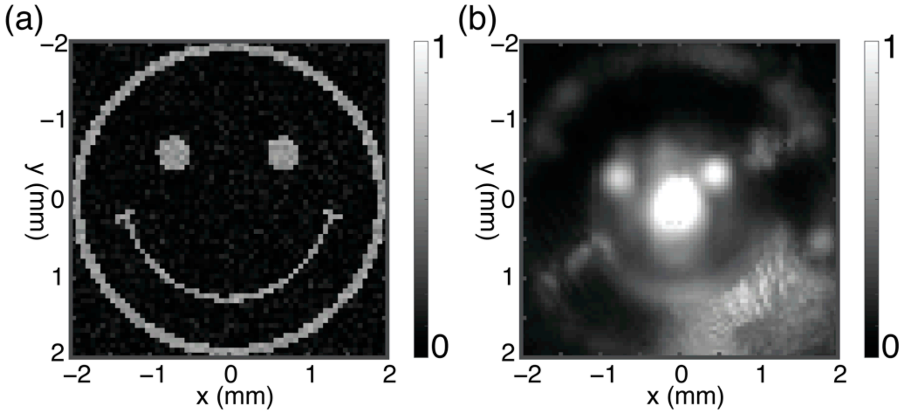

Figure 4. (**a**) Simulation results of the image after light illuminated the hologram. (**b**) Experimental results of the hologram image by using the on-axis optical setup. Note the presence of the zero order in the center of the image due to imperfect phase control.

4. Conclusions

To conclude, we have realized functional holograms at mid-infrared frequency utilizing Si nanopillars on gold substrate in order to address the 0–2π-phase modulation of the reflected field. Our eight-level discretized computer-generated phase hologram, based on a Fourier transform algorithm for high computation speed and low data storage, has been fabricated using electron beam lithography and experimentally measured, showing for the first time a holographic image at wavelength 4.7 µm, which agrees well with our calculation. The total efficiency of our metasurface-based hologram is 81%. This holographic method can be further applied to design optical elements in mid-infrared wavelengths for imaging and sensing, and can be further embedded or combined with active optical devices such as mid-infrared quantum-cascade lasers, to control both light emission and achieve optical thermal management.

Author Contributions: K.W. conceived the idea of this study. P.G. and Q.W. directed the research. K.W. performed the simulation and experimental demonstration. N.K. assisted with the experimental test. H.Q. performed the fabrication. K.W., H.Q. and P.G. prepared the manuscript. H.W. and Q.W. supervised the resources. All of the authors discussed the results and commented on the manuscript. All authors have read and agreed to the published version of the manuscript.

Funding: This research was funded by National Natural Science Foundation of China (NSFC) (Grant Nos. 11504243, 11734012), Natural Science Foundation of Jiangsu Province, China, (Grant No. BK20191282).

Acknowledgments: P.G. gratefully acknowledges financial support from the European Research Council (ERC) under the European Union's Horizon 2020 research and innovation programme (grant agreement FLATLIGHT No. 639109). K. Wu is also supported by the Fundamental Research Funds for the Central Universities (Nos. 30919011250, 30918011337).

Conflicts of Interest: The authors declare no competing interests.

References

1. Yu, N.; Genevet, P.; Kats, M.A.; Aieta, F.; Tetienne, J.-P.; Capasso, F.; Gaburro, Z. Light propagation with phase discontinuities: Generalized laws of reflection and refraction. *Science* **2011**, *334*, 333. [CrossRef] [PubMed]
2. Neshevand, D.; Aharonovich, I. Optical metasurfaces: New generation building blocks for multi-functional optics. *Light Sci. Appl.* **2018**, *7*, 58. [CrossRef]
3. Genevet, P.; Capasso, F.; Aieta, F.; Khorasaninejad, M.; Devlin, R. Recent advances in planar optics: From plasmonic to dielectric metasurfaces. *Optica* **2017**, *4*, 139. [CrossRef]

4. Parsons, J.; Hendry, E.; Burrows, C.P.; Auguie, B.; Sambles, J.R.; Barnes, W.L. Localized surface-plasmon resonances in periodic nondiffracting metallic nanoparticle and nanohole arrays. *Phys. Rev. B* **2009**, *79*, 073412. [CrossRef]
5. de Abajo, F.J.G. Colloquium: Light scattering by particle and hole arrays. *Rev. Mod. Phys.* **2007**, *79*, 1267. [CrossRef]
6. Lalanne, P.; Astilean, S.; Chavel, P.; Cambril, E.; Launois, H. Design and fabrication of blazed binary diffractive elements with sampling periods smaller than the structural cutoff. *JOSA A* **1999**, *16*, 1143. [CrossRef]
7. Huang, L.; Chen, X.; Muhlenbernd, H.; Li, G.; Bai, B.; Tan, Q.; Jin, G.; Zentgraf, T.; Zhang, S. Dispersionless Phase Discontinuities for Controlling Light Propagation. *Nano Lett.* **2012**, *12*, 5750. [CrossRef] [PubMed]
8. Yu, N.; Capasso, F. Flat optics with designer metasurfaces. *Nat. Mater.* **2014**, *13*, 139. [CrossRef]
9. Aieta, F.; Genevet, P.; Yu, N.; Kats, M.A.; Gaburro, Z.; Capasso, F. Out-of-Plane Reflection and Refraction of Light by Anisotropic Optical Antenna Metasurfaces with Phase Discontinuities. *Nano Lett.* **2012**, *12*, 1702. [CrossRef]
10. Jahani, S.; Jacob, Z. All-dielectric metamaterials. *Nat. Nanotechnol.* **2016**, *11*, 23. [CrossRef]
11. Lin, D.; Fan, P.; Hasman, E.; Brongersma, M.L. Dielectric gradient metasurface optical elements. *Science* **2014**, *345*, 298. [CrossRef] [PubMed]
12. Kuznetsov, A.I.; Miroshnichenko, A.E.; Fu, Y.H.; Zhang, J.; Luk'yanchuk, B. Magnetic light. *Sci. Rep.* **2012**, *2*, 492. [CrossRef] [PubMed]
13. Decker, M.; Staude, I.; Falkner, M.; Dominguez, J.; Neshev, D.N.; Brener, I.; Pertsch, T.; Kivshar, Y.S. High-Efficiency Dielectric Huygens' Surfaces. *Adv. Opt. Mater.* **2015**, *3*, 813. [CrossRef]
14. Arbabi, A.; Horie, Y.; Bagheri, M.; Faraon, A. Dielectric metasurfaces for complete control of phase and polarization with subwavelength spatial resolution and high transmission. *Nat. Nanotechnol.* **2015**, *10*, 937. [CrossRef]
15. Kruk, S.; Hopkins, B.; Kravchenko, I.I.; Miroshnichenko, A.; Neshev, D.N.; Kivshar, Y.S. Invited Article: Broadband highly efficient dielectric metadevices for polarization control. *APL Photonics* **2016**, *1*, 030801. [CrossRef]
16. Khorasaninejad, M.; Ambrosio, A.; Kanhaiya, P.; Capasso, F. Broadband and chiral binary dielectric meta-holograms. *Sci. Adv.* **2016**, *2*, e1501258. [CrossRef]
17. Aieta, F.; Genevet, P.; Kats, M.A.; Yu, N.; Blanchard, R.; Gaburro, Z.; Capasso, F. Aberration-Free Ultrathin Flat Lenses and Axicons at Telecom Wavelengths Based on Plasmonic Metasurfaces. *Nano Lett.* **2012**, *12*, 4932. [CrossRef]
18. Lin, R.J.; Su, V.-C.; Wang, S.; Chen, M.K.; Chung, T.L.; Chen, Y.H.; Kuo, H.Y.; Chen, J.-W.; Chen, J.; Huang, Y.-T.; et al. Achromatic metalens array for full-colour light-field imaging. *Nat. Nanotechnol.* **2019**, *14*, 227. [CrossRef]
19. Cong, L.; Xu, N.; Gu, J.; Han, J.; Zhang, W. Highly flexible broadband terahertz metamaterial quarter-wave plate. *Laser Photonics Rev.* **2014**, *8*, 626. [CrossRef]
20. Yu, N.; Aieta, F.; Genevet, P.; Kats, M.A.; Gaburro, Z.; Broadband, F.C.A. Background-Free Quarter-Wave Plate Based on Plasmonic Metasurfaces. *Nano Lett.* **2012**, *12*, 6328. [CrossRef]
21. Huang, L.; Chen, X.; Muhlenbernd, H.; Zhang, H.; Chen, S.; Bai, B.; Tan, Q.; Jin, G.; Cheah, K.; Qiu, C.; et al. Three-dimensional optical holography using a plasmonic metasurface. *Nat. Commun.* **2013**, *4*, 2808. [CrossRef]
22. Wang, L.; Kruk, S.; Tang, H.; Li, T.; Kravchenko, I.; Neshev, D.N.; Kivshar, Y.S. Grayscale transparent metasurface holograms. *Optica* **2016**, *3*, 1504. [CrossRef]
23. Wang, B.; Dong, F.; Li, Q.-T.; Yang, D.; Sun, C.; Chen, J.; Song, Z.; Xu, L.; Chu, W.; Xiao, Y.-F.; et al. Visible-Frequency Dielectric Metasurfaces for Multiwavelength Achromatic and Highly Dispersive Holograms. *Nano Lett.* **2016**, *16*, 5235. [CrossRef]
24. Genevet, P.; Capasso, F. Holographic optical metasurfaces: A review of current progress. *Rep. Prog. Phys.* **2015**, *78*, 024401. [CrossRef]
25. Brown, B.R.; Lohmann, A.W. Complex Spatial Filtering with Binary Masks. *Appl. Opt.* **1966**, *5*, 967. [CrossRef]
26. Bohren, C.F.; Huffman, D.R. *Absorption and Scattering of Light by Small Particles*; Wiley: New York, NY, USA, 1983.
27. Taflove, A.; Hagness, S.C. *Computational Electrodynamics: The Finite-Difference Time-Domain Method*, 3rd ed.; Artech House: Norwood, MA, USA, 2000.

28. Helgert, C.; Menzel, C.; Rockstuhl, C.; Pshenay-Severin, E.; Kley, E.-B.; Chipouline, A.; Tünnermann, A.; Lederer, F.; Pertsch, T. Polarization-independent negative-index metamaterial in the near infrared. *Opt. Lett.* **2009**, *34*, 704. [CrossRef]
29. Li, T.; Wang, S.; Zhang, X.-L.; Deng, Z.-L.; Hang, Z.H.; Sun, H.-B.; Wang, G.P. Non-uniform annular rings-based metasurfaces for high-efficient and polarization-independent focusing. *App. Phys. Lett.* **2015**, *107*, 251107. [CrossRef]
30. Schmitt, N.; Georg, N.; Briere, G.; Loukrezis, D.; Heron, S.; Lanteri, S.; Klitis, C.; Sorel, M.; Romer, U.; Gersem, H.D.; et al. Optimization and uncertainty quantification of gradient index metasurfaces [Invited]. *Opt. Mater. Express* **2019**, *9*, 892. [CrossRef]
31. So, S.; Rho, J. Designing nanophotonic structures using conditional deep convolutional generative adversarial networks. *Nanophotonics* **2019**, *8*, 12551261. [CrossRef]
32. Ong, J.R.; Chu, H.S.; Chen, V.H.; Zhu, A.Y.; Genevet, P. Freestanding dielectric nanohole array metasurface for mid-infrared wavelength applications. *Opt. Lett.* **2017**, *42*, 2639. [CrossRef]
33. Elsawy, M.M.R.; Lanteri, S.; Duvigneau, R.; Briere, G.; Mohamed, M.S.; Genevet, P. Global optimization of metasurface designs using statistical learning methods. *Sci. Rep.* **2019**, *9*, 17918. [CrossRef]
34. Peurifoy, J.; Shen, Y.; Jing, L.; Yang, Y.; Cano-Renteria, F.; DeLacy, B.G.; Joannopoulos, J.D.; Tegmark, M.; Soljacic, M. Nanophotonic particle simulation and inverse design using artificial neural networks. *Sci. Adv.* **2018**, *4*, eaar4206. [CrossRef]
35. Jiang, J.; Fan, J.A. Global Optimization of Dielectric Metasurfaces Using a Physics-Driven Neural Network. *Nano Lett.* **2019**, *19*, 5366. [CrossRef]